Journal of Materials Chemistry C

Materials for optical, magnetic and electronic devices

rsc.li/materials-c

ROYAL SOCIETY
OF CHEMISTRY
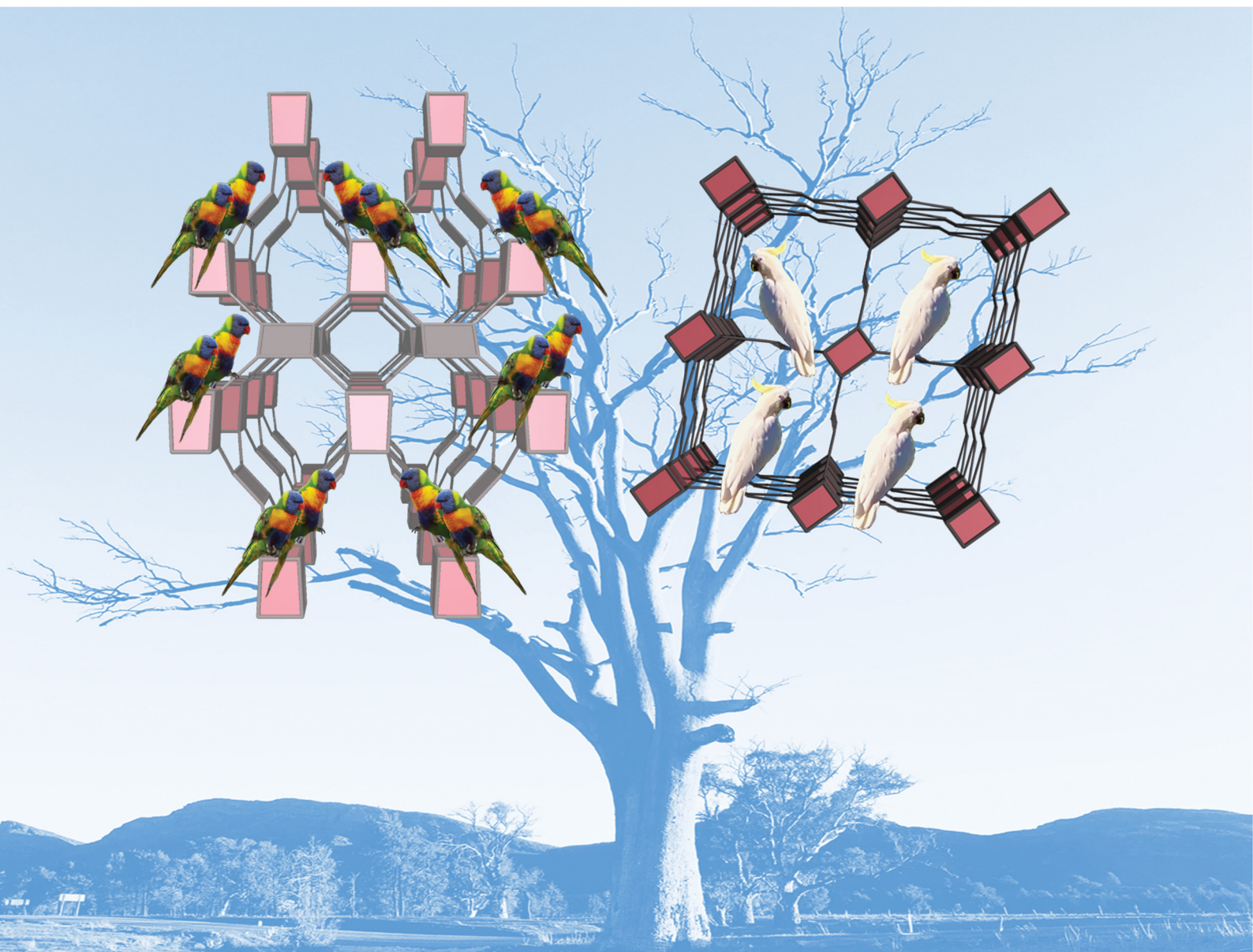
PAPER
Jack D. Evans, Christian J. Doonan, Christopher J. Sumby *et al*.
Topological analysis and control of post-synthetic metalation
sites in Zr-based metal–organic frameworks

Topological analysis and control of post-synthetic metalation sites in Zr-based metal–organic frameworks†

Pol Gimeno-Fonquernie, [ID] [a] Jorge Albalad, [ID] ‡ [a] Jason R. Price, [b] Witold M. Bloch, [ID] [c] Jack D. Evans, [ID] * [a] Christian J. Doonan [ID] * [a] and Christopher J. Sumby [ID] * [a]

The design criteria needed for the formation of the **sqc** metal–organic framework (MOF) topology, from an 8-connecting node and a 4-connecting linker, are unclear due to a limited number of reports. After recently reporting the MOF UAM-1000 (UAM = University of Adelaide Material), which has this rare sqc topology, we present a study that explores the effect of flexible tetrapyrazole carboxylate linker structure metrics on the topology of Zirconium-based MOFs (Zr-MOFs). By modifying the linker length and width, three new Zr-MOFs (UAM-10, UAM-11, and UAM-1002) were synthesized and characterized. The study reveals that linker dimensions influence the accessible conformations, and along with fine-tuning of synthetic conditions, allow control over MOF topology. Additionally, linker flexibility plays a crucial role in the formation of the **sqc** over the more common **csq** topology. Finally, the presence of free bis-pyrazolyl groups in the reported MOFs allowed us to evaluate the potential for post-synthetic metalation (PSMet). UAM-10 and UAM-11 are too rigid, the pyrazole groups lack the appropriate arrangement and therefore these materials do not undergo PSMet. In contrast, UAM-1002 with its **scu** topology exhibits the right quanta of flexibility needed for successful PSMet, making it a promising platform for studying the chemistry of anchored organometallic complexes. Moreover, the different topology for UAM-1002 *versus* UAM-1000 changes the nature of the PSMet site (bidentate *versus* a tetradentate site) despite these being made from the same node and linker building blocks.

Introduction

The topology of a metal–organic framework (MOF), namely the type of network structure, plays a crucial role in determining its stability, and its adsorption, separation, and catalytic properties.[1–4] Different topologies result in distinct pore shapes

[a] *Centre for Advanced Nanomaterials and Department of Chemistry, School of Physics, Chemistry and Earth Sciences, The University of Adelaide Adelaide, SA 5005, Australia. E-mail: j.evans@adelaide.edu.au, christian.doonan@adelaide.edu.au, christopher.sumby@adelaide.edu.au*

[b] *ANSTO Melbourne, The Australian Synchrotron, 800 Blackburn Rd, Clayton, Vic 3168, Australia*

[c] *College of Science & Engineering, Flinders University, Sturt Road, Bedford Park, SA 5042, Australia*

and sizes that can significantly impact guest adsorption and selectivity of the MOF toward particular adsorbates.[5] Similarly, topology can determine substrate and product diffusion rates and thereby catalytic properties.[6,7] Despite extensive research on the reticulation of MOFs and the development of the secondary building block (SBU) approach[7–9] to MOF design, with the exception of highly connected SBUs,[10] predicting MOF structures remains a challenge as multiple net topologies exist for a given combination of metal node and link geometries.[11–13] Therefore, understanding topological control in MOFs is crucial to provide phase pure samples and ensure the topology with the most suitable performance characteristics is obtained.[14]

Zirconium (Zr) based MOFs have attracted increasing interest since their 2008 discovery due to the exceptional strength of the Zr–O bond, which enables the formation of highly stable and robust materials.[15–17] The typical Zr cluster consists of six Zr atoms forming an octahedron that can coordinate up to 12 carboxylate groups, resulting in a wide variety of topologies with 4, 5, 6, 8, 10, and 12-connected clusters.[11] Several studies have provided understanding of the different connectivities of Zr clusters.[18] For instance, the formation of the **ftw** topology,
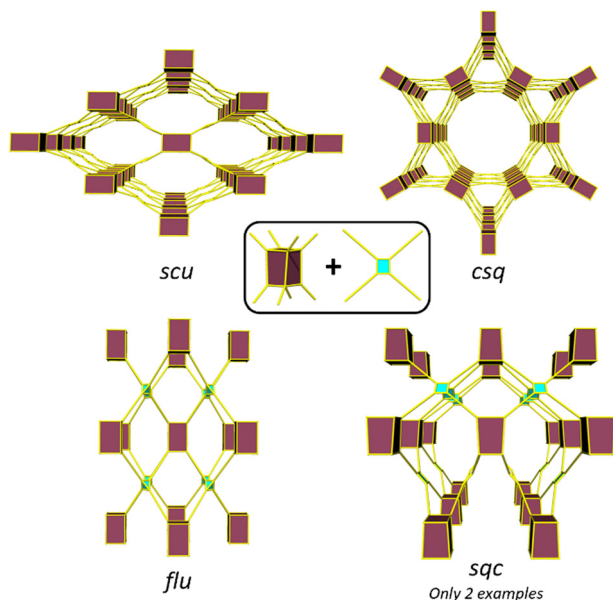
Fig. 1 Representations of the four different topologies that can be formed from a cubic 8-connected cluster and a tetratopic linker (with either a tetrahedral or square planar geometry). The maroon polyhedron represents the cluster and the blue shaded rectangle or polygon with yellow lines represents the organic linker.

formed by the combination of a 12-connected cluster and a square linker, is only possible with square linkers where the oxygen atoms of the carboxylate groups are in plane with the core of the linker.[19] The use of a rectangular linkers, substituents or bulky ligands to induce an out-of-plane arrangement of the carboxylate groups leads to the formation of an 8-connected cluster.[20] In some of these cases, different topologies can be possible from the same metal cluster and linker connectivity, and control of Zr MOF topology becomes more challenging. An illustrative example is the reaction of the cubic 8-connected Zr-cluster with a tetratopic linker, which can lead to the formation of four different topologies: **flu** when the linker adopts a tetrahedral arrangement of the donors and **csq**, **scu**, and **sqc** when the linker adopts a planar conformation (Fig. 1). Several studies have probed the factors, such as the presence of bulky substituents in the organic linker,[21,22] synthetic conditions,[23,24] modulator rigidity and co-modulator acidity,[25] that can influence the formation of different topologies. Furthermore, in certain cases, the addition of a seed of a phase pure MOF has been shown to be required for the synthesis of a particular MOF, while the absence often leads to the formation of a mixture of phases.[26]

Despite the existence of at least four possible topologies from reacting a cubic 8-connected Z-cluster with a tetratopic linker, previous studies have mainly focused on differentiating between the formation of the **flu**, **scu** and **csq** topologies.[21–24] This is primarily due to the rarity of MOFs with the **sqc** topology, with only two reported examples to date.[27,28] Notably, our group only recently communicated the second synthesis of a MOF with the **sqc** topology (UAM-1000).[28] In this MOF and braced analogues (UAM-1001), a flexible linker containing free

bis-pyrazolyl groups allows for post-synthetic metalation (PSMet) with dinuclear complexes. PSMet is a widely applied technique that allows the functionalization of MOFs with secondary, often non-structural metal centres, conferring MOFs with novel physical, optical, sorption and catalytic properties. Given that Zr-MOFs based on tetratopic carboxylate linkers can access different topologies, control over MOF topology can therefore be used to dictate the outcome of PSMet as the spatial disposition of the metalation sites can lead to the isolation of different metalation products.

To enhance our understanding of the synthesis of Zr-MOFs for PSMet, and provide insights into the formation of the **sqc** topology in UAM-1000, this study investigates the effect of flexible tetrapyrazole carboxylate linker metrics on MOF topology. Starting from the linker 1,1,2,2-tetrakis[4-(4-carboxyphenyl)-1*H*-pyrazol-1-yl]ethane (TCPE), which was used to form UAM-1000, we modified the length and width of the linker, resulting in two new linkers: 1,1'-methylenebis(1*H*-pyrazole-4-carboxylic acid) (L1H$_4$) and 1,4-bis(bis(4-carboxy-1*H*-pyrazol-1-yl)methyl)benzene (L2H$_4$). Each linker, including TCPE, was reacted with ZrCl$_4$ under different conditions to evaluate the formation of different topologies, allowing an assessment of the characteristics needed to form the different MOFs and the effect of MOF topology on PSMet outcome. Overall, the study reports the synthesis and characterization of three new Zr-MOFs (UAM-10, UAM-11, and UAM-1002), each containing non-coordinated bis-pyrazolyl units, and investigates their potential for PSMet, showing the ability to form metalation sites for discrete mononuclear and dinuclear complexes.

Experimental section

Materials and methods

Unless otherwise stated, all chemicals were obtained from commercial sources and used as received. 1,1,2,2-Tetrakis-[4-(4-carboxyphenyl)-1*H*-pyrazol-1-yl]ethane[29,30] and 1,4-bis(dibromomethyl)benzene[31] were synthesized following an already reported procedure. Acetonitrile (MeCN) was dried from CaH$_2$ under N$_2$ and degassed with Ar prior to use.

Powder X-ray diffraction (PXRD) data were collected on a Bruker Advanced D8 diffractometer (capillary stage) using Cu Kα radiation (λ = 1.5456 Å, 40 kW/40 mA, 2θ = 2–52.94°, φ rotation = 20 rotations per min, at 1 s exposure per step with 5001 steps, and using 0.5 mm glass capillaries). Fourier Transform Infrared Spectroscopy (FTIR) spectra were collected on a Shimadzu IR spirit using ATR mode (spectral range: 7800–350 cm^{-1}). Nuclear Magnetic Resonance (NMR) spectra were collected at 25 °C in deuterated solvents on an Agilent DD2 500 MHz NMR with a 5 mm OneNMR probe, using tetramethylsilane (TMS) signals as the internal reference standard. Scanning Electron Microscopy (SEM) images were collected, and Energy Dispersive X-ray (EDX) analysis performed on a FEI Quanta 450 field-emission scanning electron microscope, operating at 10.0–20.0 kV and under ultra-high vacuum (10^{-7}–10^{-12} hPa) conditions. The samples were prepared for

2360 | *J. Mater. Chem. C*, 2024, **12**, 2359–2369

This journal is © The Royal Society of Chemistry 2024

analysis by mounting a mixture of intact and crushed crystals on the SEM stub, measuring the metal composition for areas of the sample, and averaging the measurements. Gas adsorption measurements were performed on a Micromeritics 3-Flex surface area and pore size analyser. Activation conditions for each sample is stated in figure captions (Fig. S10, S15, S21, S30–S32, ESI†). Thermogravimetric analysis data was collected on an STA 449 F3 Jupiter analyser from 45–700 °C at 5 °C min^{-1} under 21% O_2, 79% N_2.

Molecular simulations

The ligands L1, L2 and L3 were considered as the corresponding acid and the conformational landscape was assessed using the Conformer-Rotamer Ensemble Sampling Tool (CREST)[32] with an energy window of 30 kJ mol^{-1} and energies computed using GFN2-xTB[33] with implicit solvation of DMF considered by the analytical linearized Poisson–Boltzmann approach.[34]

Framework models were produced using the weaver code[35] and resulting frameworks first optimised using the UFF[36] as implemented by the lammps-interface[37] using the lammps simulation engine.[38] Subsequently, the geometry and cell parameters for these frameworks were optimised using density functional theory (DFT). These calculations used the PBE functional,[39] Goedecker-Teter-Hutter pseudopotential[40] and D3 London dispersion corrections,[41] together with a double-zeta valence (DZVP) basis set. A grid cutoff of 800 Ry was employed and a relative cutoff of 70 Ry. The DFT approach used the QUICKSTEP[42] module of the CP2K program package.[43] Pore metrics of these frameworks were computed using the Zeo + + software package.[44] Frameworks based on different *anti–anti* or *syn–syn* ligand conformations were considered at the classical level of theory (UFF) and the framework was constructed based on the lowest energy conformer observed with *anti–anti* or *syn–syn* arrangement.

Single crystal X-ray diffraction

Single crystals were mounted in Paratone-N oil on a MiTeGen micromount. Single-crystal X-ray data of UAM-10, UAM-11 and UAM-1002 were collected at 100 K on the MX1 or MX2 beamlines of the Australian Synchrotron using the Blue-ice software interface,[45] λ = 0.71073 Å and absorption corrections were applied using multiscan methods using XDS.[46,47] UAM-1002[PdCl2] was collected at 100 K on a Rigaku XtaLAB Synergy-s diffractometer equipped with a HyPix-6000HE detector. The structures were solved using SHELXS or SHELXT,[48,49] and refined by full-matrix least squares on F^2 by SHELXL,[50] interfaced through the program X-Seed or OLEX.[51,52] In general, all atoms were refined anisotropically and hydrogens atoms were included as invariants at geometrically estimated positions, unless specified otherwise in additional details in ESI.† Where noted, the data was treated with the SQUEEZE routine available in Platon[53] or using the solvent masking feature of Olex. Images were produced using the software Diamond Version 4.6.8.[54] X-ray experimental data is given in Table S5 (ESI†). CIF data have been deposited with the Cambridge Crystallographic Data Centre,

CCDC reference numbers CCDC 2288076–2288079 (2288076 = UAM-10; 2288077 = UAM-11; 2288079 = UAM-1002; 2288078 = UAM-1002[PdCl2]).†

Synthetic protocols

Synthesis of 1,1′-methylenebis(1H-pyrazole-4-carboxylic acid) (L1H4). Ethyl 1H-pyrazole-4-carboxylate (5.1 g, 0.036 mmol) and potassium carbonate (2.0 g, 0.036 mmol) were dissolved in 10 mL of DMSO, and the resulting solution was stirred for 1 h at 80 °C. After that, a solution of 1,1,2,2-tetrabromoethane (1.16 mL, 0.010 mmol) in 15 mL of DMSO was added dropwise before being left to stir overnight at 80 °C. The mixture was cooled to room temperature and poured into water (250 mL) to precipitate a white solid. The solid was collected, washed with water and 3 : 7 ethanol/water, and dried in air to give the ester-protected compound. Deprotection was achieved by boiling the white solid in 1 M NaOH overnight. The resulting solution was acidified with 4 M HCl to pH 2 to precipitate H4L1 as a white solid, which was subsequently collected, washed with water and acetone, and dried under vacuum overnight. Yield: 1.8 g (40%). ^{1}H NMR (500 MHz, DMSO-d_6): 12.62 (s, 4H, COOH), 8.69 (s, 4H, CH$_2$ pyrazole), 8.52 (s, 2H, N–CH–N), 7.84 (s, 4H, CH$_2$ pyrazole). ^{13}C-NMR spectrum (500 MHz, DMSO-d_6): 162.98 (COOH), 141.86 (C pyr), 134.76 (C pyr), 116.03 (C py), 71.98 (C-sp^3). MS (ESI†): calcd for $C_{18}H_{13}N_8O_8^+$ [M]$^+$ 469.08, found 469.08.

Synthesis of 1,4-bis(bis(4-carboxy-1H-pyrazol-1-yl)methyl)-benzene (L2H4). Ethyl 1H-pyrazole-4-carboxylate (5.1 g, 0.036 mmol) and potassium carbonate (2.0 g, 0.036 mmol) were dissolved in 10 mL of DMSO, and the resulting solution was stirred for 1 h at 80 °C. After that, a solution of 1,4-bis(dibromomethyl)benzene (4.21 g, 0.010 mmol) in 15 mL of DMSO was added dropwise before being left to stir overnight at 80 °C. The mixture was cooled to room temperature and poured into water (250 mL) to precipitate a white solid. The solid was collected, washed with water and 3 : 7 ethanol/water, and dried in air to give the ester-protected compound. Deprotection was achieved by boiling the white solid in 1 M NaOH overnight. The resulting solution was acidified with 4 M HCl to pH 2 to precipitate H4L2 as a yellow solid, which was subsequently collected, washed with water and acetone, and dried under vacuum overnight. Yield: 1.08 g (22%).^{1}H NMR (500 MHz, DMSO-d_6): 12.62 (s, 4H, COOH), 8.37 (s, 4H, CH2 pyrazole), 8.25 (s, 2H, N–CH–N), 7.98 (s, 4H, CH2 pyrazole), 7.25 (s, 4H, CH phenyl). ^{13}C-NMR spectrum (500 MHz, DMSO-d_6): 163.22 (COOH), 141.80 (COOH), 136.21 (C pyr), 134.04 (C pyr), 127.72 (C pheyl), 116.09 (s, 4H, C pyr), 75.93 (C-sp^3). MS (ESI†): calcd for $C_{24}H_{17}N_8O_8^+$ [M]$^+$ 545.12, found 545.12.

Synthesis of UAM-10. ZrCl4 (12 mg, 0.05 mmol) and H4L1 (10 mg, 0.02 mmol) were dissolved in 0.5 mL of DMF by sonicating the initial suspension (2 min). Acetic acid (0.8 mL, 14 mmol, 280 mol. eq.) was then added to the solution, and the resulting mixture was transferred to a scintillation vial, capped tightly, and heated at 120 °C for 24 h. Colourless needle shaped crystals of UAM-10 were collected by filtration and washed with DMF (4 × 5 mL), acetone (3 × 5 mL) and dried under vacuum for 24 h.

This journal is © The Royal Society of Chemistry 2024

J. Mater. Chem. C, 2024, **12**, 2359–2369 | **2361**

Synthesis of UAM-11. $ZrCl_4$ (12 mg, 0.05 mmol) and H_2L2 (10 mg, 0.018 mmol) were dissolved in 0.5 mL of DMF by sonicating the initial suspension (2 min). Acetic acid (0.5 mL, 8.74 mmol, 175 mol. eq.) was then added to the solution, and the resulting mixture was transferred to a scintillation vial, capped tightly, and heated at 120 °C for 72 h. Yellow clumps of block shaped crystals of UAM-11 were collected by filtration and washed with DMF (4 × 5 mL), acetone (3 × 5 mL) and dried under vacuum for 24 h.

Synthesis of UAM-1000. UAM-1000 was synthesized by modifying an already reported procedure.[28] Briefly, $ZrCl_4$ (12 mg, 0.05 mmol) and TCPE (10 mg, 0.018 mmol) were dissolved in 2 mL of DMF by sonicating the initial suspension (2 min). Acetic acid (0.5 mL, 8.74 mmol, 175 mol. eq.) was then added to the solution, and the resulting mixture was transferred to a scintillation vial, capped tightly, and heated at 120 °C for 72 h. Colourless octahedral crystals of UAM-1000 were collected by filtration and washed with DMF (4 × 5 mL), acetone (3 × 5 mL) and dried under vacuum for 24 h. Alternatively, UAM-1000 can be synthesized by replacing acetic acid for trifluoroacetic acid (0.3 mL, 3.92 mmol, 78 mol. eq.) or benzoic acid (300 mg, 2.46 mmol, 49 mol. eq.).

Synthesis of UAM-1002. $ZrCl_4$ (12 mg, 0.05 mmol) and formic acid (0.5 mL, 8.74 mmol, 175 mol. eq.) TCPE (10 mg, 0.018 mmol) were dissolved in 1 mL of DEF by sonicating the initial suspension (2 min) and the solution was heated to 100 °C for 1 h. A solution of TCPE (10 mg, 0.018 mmol) in DEF (1 mL) was then added, and the resulting mixture was transferred to a scintillation vial, capped tightly, and heated at 120 °C for 72 h. Colourless needle shaped crystals of UAM-1002 were collected by filtration and washed with DEF (4 × 5 mL), acetone (3 × 5 mL) and dried under vacuum for 24 h.

Synthesis of UAM-1002[PdCl₂]. UAM-1002 crystals (two batches, *ca.* 50 mg, 0.028 mmol) were soaked in 3 mL of dry acetonitrile. An excess of $PdCl_2$ (~5 mg) was added, and the solution was heated to 80 °C for 16 h. The sample was then washed by decantation with dry acetonitrile (4 × 4 mL) and with dry toluene (4 × 4 mL). The orange crystals (54 mg, quantitative) were left in solution for characterization by SCXRD. SEM-EDX molar ratio 3.0(Zr) : 2.0(Pd) : 4(Cl).

Results and discussion

Linker synthesis and preferred conformation

The new flexible tetrapyrazole carboxylate linkers, 1,1′-methylene-bis(1*H*-pyrazole-4-carboxylic acid) (L1H₄) and 1,4-bis(bis(4-carboxy-1*H*-pyrazol-1-yl)methyl)benzene (L2H₄), were synthesized using a similar two-step synthesis procedure, where ethyl 4-carboxypyrazole was coupled to 1,1,2,2-tetrabromoethane or 1,4-bis(dibromomethyl)benzene, followed by deprotection of the ester protecting groups. The synthesis of both linkers was confirmed by ¹H-NMR (Fig. S1 and S2, ESI†) and ¹³C-NMR spectroscopy (Fig. S3 and S4, ESI†), and mass spectrometry (Table S1, ESI†).

Given that at least three topologies are accessible for a cubic 8-connected cluster and a flexible rectangular tetratopic linker, simulations were employed to explore the conformational flexibility of TCPE and these new ligands, thereby unveiling their preferred conformation (Fig. 2). A series of possible and unique conformers in a relative energy window of 30 kJ mol⁻¹ were computed. The different dihedral angles of the resulting ensembles of conformers were analysed to consider the arrangement of framework forming bonds. Specifically, two sets of NNNN dihedrals were measured, which dictate the *syn* or *anti* conformation for each set of pyrazole units, and the HCCH angle that describe the relative positions of the carboxylate groups (planar or tetrahedral) was determined (Fig. 2). Analysis of the NNNN dihedral angle for each of the ligands reveals that L1H₄ and TCPE access similar conformational space (Fig. 2(a) and (c)) showing the *anti–anti* conformation of the bis-pyrazolyl units is the lowest in energy (NNNN ∼ ±180°). The longer arm length (width) of TCPE seems to facilitate the transition from *anti–anti* to *syn–syn* conformation as it shows intermediate conformers lower in energy, which suggest an easier transition. A different outcome was observed for L2H₄. Analysis of the NNNN dihedral angles for L2H₄ reveals a greater range of conformations with low energy but the perfect *syn–syn* and *anti–anti* conformations (NNNN ∼ ±180°) are not accessible owing to steric hindrance of the central phenyl ring. Conformations closed to *anti–anti* conformations (NNNN ∼ ±180°) have the lowest energy. In all cases, we observe the same trends in energy for *syn* and *anti* conformations of the pyrazole units as previously reported for a similar bispyrazole carboxylate ligand,[55] with an energy difference disfavouring the *syn*-conformations on the order of 5–10 kJ mol⁻¹.

Analysis of the HCCH angle, reveals the effect of the phenyl unit on L2H₄, where the HCCH dihedral of the central ethylene groups, which in turn dictates positions of carboxylates (planar or tetrahedral), can rotate almost without restriction. In comparison, L1H₄ and TCPE are restricted to approximately coplanar and *anti* HCCH conformations. Overall, these simulations demonstrate that a range of different conformations are possible for these flexible tetrapyrazole carboxylate linkers, but the individual bis-pyrazole units typically prefer one of two possible arrangements (*anti* preferred over *syn*). In terms of the overall linker geometry, L1H₄ and TCPE are restricted to broadly *anti* HCCH conformations but the phenyl spacer of L2H₄ provides even greater conformational flexibility. Based on the restricted flexibility seen in the conformational modelling, it is anticipated that certain MOF topologies should be favoured by the three ligands, with the **flu** topology likely to be accessible for L2H₄, but L1H₄ and TPCE likely restricted to the **csq**, **scu**, and **sqc** topologies (*e.g.*, UAM-1000, based on TCPE, adopts the **sqc** topology).

MOF synthesis and structures

With this information in hand, we investigated the synthesis of MOFs with the two new linkers. Reaction of L1H₄ with $ZrCl_4$ using an acetic acid (AcOH) modulator in dimethylformamide (DMF) yielded colourless needle-shaped crystals corresponding
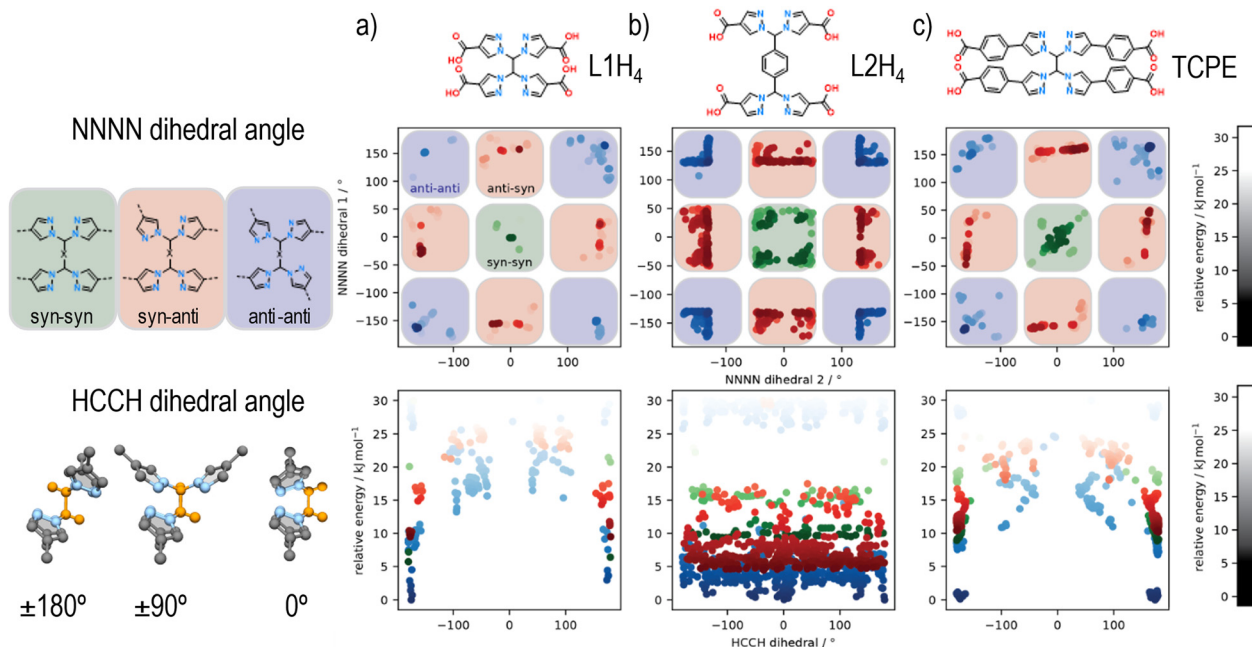
Fig. 2 Plots of the simulation output showing the relative energy of different conformations of L1H$_4$, L2H$_4$ and TCPE upon changing the NNNN dihedral angle of the bis-pyrazolyl groups (top row) and the HCCH dihedral angle of the ethylene bridge (bottom row), the latter for each of the three conformations accessible by changing the NNNN dihedral angle. Colour intensity is indicative of the relative energy, with darker colours being lower in energy and lighter colours higher in energy. On the left of the plots are representations of the conformations accessed upon changing each of the dihedral angles. In the representation of the HCCH dihedral angle (bottom-left), the H and C atoms are highlighted in orange. The Y-axis label is shared across plots within the same row.

to a MOF with a chemical formula of [Zr$_6$(μ_3-OH)$_8$(μ_2-CH$_3$COO)$_4$(L1)$_2$] (UAM-10) (Fig. S5, ESI†). SCXRD revealed the MOF to have a 3D structure that consists of an 8-connected octahedral Zr$_6$ cluster forming the common cubic SBU (Fig. 3). L1 adopts a rectangular geometry where all four carboxylate groups sit in a plane, as suggested by calculations, connecting four Zr-SBUs. The 3D structure has an **scu** topology with 17.0 by 15.8 Å rhombic channels that are accessible along the c axis (Fig. 3 and Fig. S6, ESI†). The proximity of the Zr-clusters in the c-axis leads to these being bridged by acetate groups (Fig. S7, ESI†) forming a rod-type MOF (and a different topology when these are considered in the analysis).[4] PXRD analysis of a bulk sample of UAM-10 confirmed phase purity (Fig. S8, ESI†). Thermogravimetric analysis (TGA), after activation under vacuum at room temperature, reveals thermal stability up to 350 °C (Fig. S9, ESI†) typical of Zr-MOFs. A 77K N$_2$ adsorption isotherm of UAM-10 after activation shows the material to be porous to nitrogen with a type I isotherm, a Brunauer–Emmett–Teller (BET) surface area of 864 m^2 g^{-1} (Fig. S10, ESI†) and a total pore volume of 0.28 cm^3 g^{-1}.

Reaction of L2H$_4$, which possesses the phenyl spacer that leads to decoupling of the bis-pyrazole units, with ZrCl$_4$ and an AcOH modulator in DMF yielded pale yellow crystals corresponding to a MOF with a chemical formula of [Zr$_6$(μ_3-OH)$_8$(μ_2-CH$_3$COO)$_4$(L2)$_2$] (UAM-11) (Fig. S11, ESI†). UAM-11 also has the cubic 8-connected SBUs with each L2 connecting four Zr SBUs. However, in this case, L2 adopts a tetrahedral geometry to form a **flu** topology (Fig. 3 and Fig. S12, ESI†) as might be anticipated

from the analysis of preferred conformations. Phase purity of the sample was confirmed by PXRD (Fig. S13, ESI†) and TGA also reveals thermal stability up to 350 °C (Fig. S14, ESI†). A 77K N$_2$ adsorption isotherm of UAM-11 after activation shows the material to be porous to nitrogen with a type I isotherm, a BET surface area of 844 m^2 g^{-1} (Fig. S15, ESI†) and a total pore volume of 0.27 cm^3 g^{-1}. Despite the ligand length being increased from L1 to L2, the greater flexibility of L2 facilitates access to the more dense **flu** topology and thereby a similar BET surface area and total pore volume.

The formation of UAM-1000 as the product of the reaction of TCPE with ZrCl$_4$ using trifluoroacetic acid (TFA) as modulator in DMF was recently reported by our group.[28] The synthesis was reported using TFA as modulator. As the use of different solvents and modulators could lead to different topologies, we reinvestigated the synthesized UAM-1000. Using AcOH as the modulator, UAM-1000AA (acetic acid) was formed and PXRD analysis confirmed the formation of UAM-1000 as the sole product (Fig. S16, ESI†). Briefly, UAM-1000 consists of the cubic Zr-SBU with each linker connecting four Zr-SBUs to form a MOF with **sqc** topology (Fig. 3, 2nd example reported).[8,27] UAM-1000 can also be synthesized in DMF in using benzoic acid (BA) (UAM-1000BA) and TFA (UAM-1000TFA) as confirmed by PXRD (Fig. S16, ESI†). However, a different structure and topology is formed when using both DEF as the solvent and formic acid (FA) as the modulator; using FA in DMF only gives amorphous material. Using the other modulators (AA, BA, and TFA) in DEF also gives amorphous material except in the case of BA
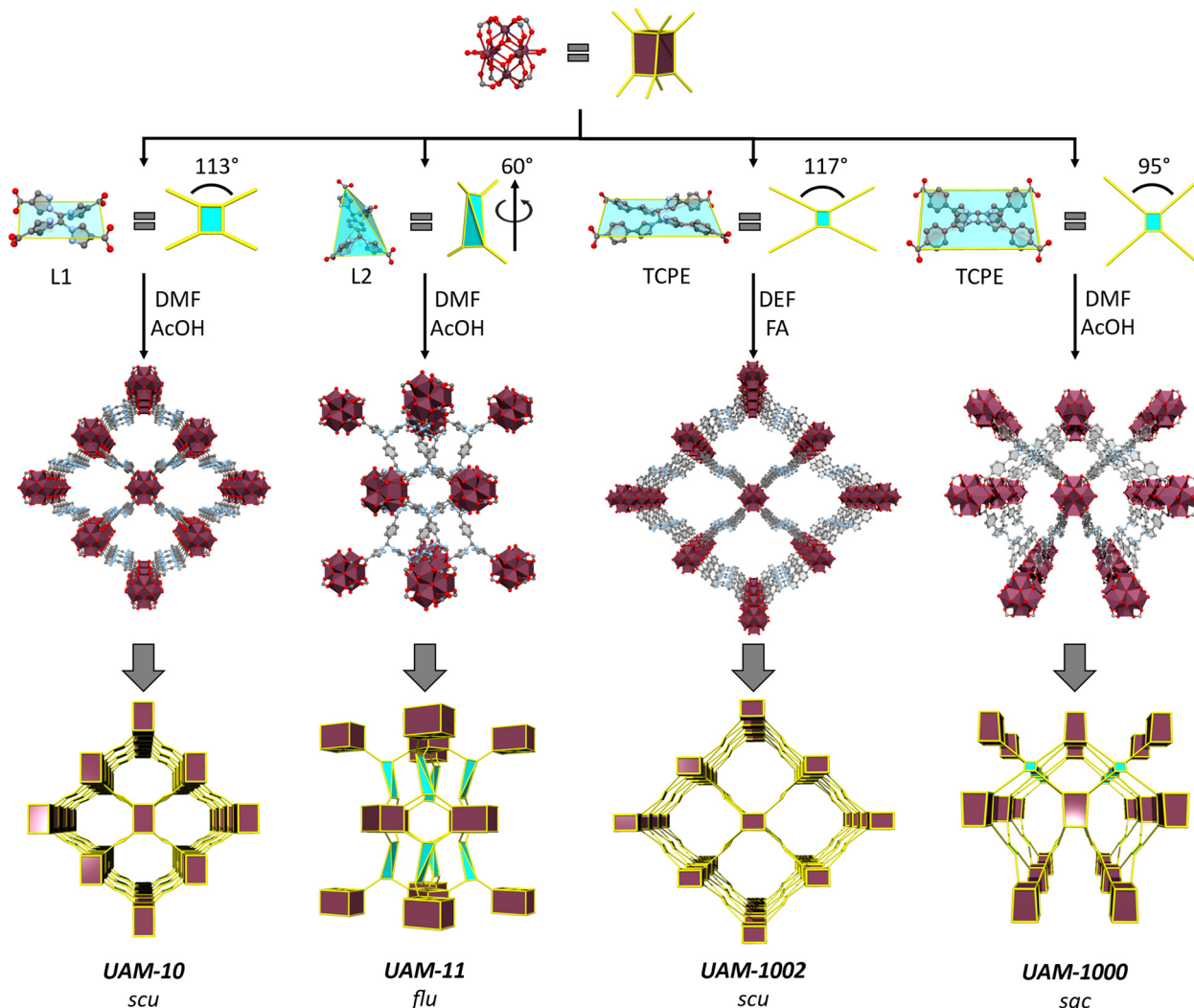
Fig. 3 A summary of the synthesis, structure and topologies of UAM-10, UAM-11, UAM-1002 and UAM-1000. All four MOFs are formed from the same 8-connected cubic Zr-cluster but different linkers and linker conformations lead to the formation of different MOF topologies, in part governed by the restrictions on linker flexibility. The maroon polyhedron represents the cluster and the blue shaded rectangle/polyhedron with yellow lines represents the organic linker.

which leads to the formation of the **sqc** topology (UAM-1000). Reaction of TCPE with $ZrCl_4$ in the presence of DEF using FA as modulator provides UAM-1002, which forms as large colourless needle-shaped crystals that could be characterized by SCXRD (Fig. S17, ESI†). Structure solution and refinement by SCXRD revealed the formation of a MOF with an **scu** topology, like UAM-10, but where the Zr clusters are not bridged by the carboxylate group of the modulator (Fig. 3 and Fig. S18, ESI†).

PXRD analysis of bulk UAM-1002 confirmed phase purity of the samples (Fig. S19, ESI†). Thermogravimetric analysis (TGA) analysis, after activation under vacuum at room temperature, reveals thermal stability up to 475 °C (Fig. S20, ESI†). A 77K N_2 adsorption isotherm of UAM-1002 after thermal activation shows a BET surface area of 138 m^2g^{-1} (Fig. S21, ESI†) and a total pore volume of 0.04 cm^3 g^{-1}. These values are considerably lower than expected based on calculations conducted on the crystal structure (3400 m^2 g^{-1} and 1.14 cm^3 g^{-1}). Activation

under supercritical CO_2 showed a slight increase in porosity with a BET of 567 m^2 g^{-1} (Fig. S21, ESI†) and a total pore volume of 0.18 cm^3 g^{-1}. However, this remained much lower than the calculated values. We hypothesize that the larger pore volume and anticipated flexibility of UAM-1002 is allowing partial collapse of the structure upon activation. PXRD data (Fig. S22, ESI†) for activated UAM-1002 (UAM-1002·activated) shows peaks associated with *hkl* planes (0,2,0), (0,0,1) and (2,0,0) shift compared to those in as-synthesised UAM-1002. We could not determine the activated structure by SCXRD but the PXRD changes, and the loss of accessible pore volume, is consistent with a transition to a closed phase, as is observed with other similar MOFs (*e.g.* MIL-53 type MOFs, CuMOF-1).[56–58]

Topologies of UAM-10, UAM-11, UAM-1002 and UAM-1000

Zr clusters with 4, 5, 6, 8, 10, and 12-connected SBUs have been reported, but the 8 and 12-connected examples are the most

common. Thus, we will focus on possible topologies with the 8-connected Zr-SBU (cubic) and the 12-connected SBU (cuboctahedra), and considering that all linkers used are tetratopic linkers, only six topologies are possible. Among the six topologies, **ftw** is only accessed with a planar linker and a cuboctahedral SBU, **ith** is the only combination for a tetrahedral linker and a cuboctahedral SBU, and **flu** is the only possibility of a tetrahedral linker and the cubic SBU. Finally, three possible topologies can be formed with a cubic SBU and a planar linker: **csq**, **scu**, and the less common **sqc**.

To understand the linker preferences for different topologies we produced hypothetical models for each framework. We used single conformation of each ligand (based on the lowest energy conformer discovered above) and arranged these to produce likely framework structures for each of the six possible topologies. There are an immense number of combinations of inorganic node and ligand orientations[59] but here only a single representative framework was produced to provide a reasonable model for each topology and ligand. We note, the production of framework models of complex topologies, where there a many possible linker orientations and conformations, are challenging and require exhaustive search approaches.[35] In this study a single arrangement of the ligands with a single conformation were considered. As a result, these hypothetical frameworks serve as a simple guide of the energy landscape for these topologies.

The **ftw** topology is edge-transitive and, as noted, based on a cuboctahedral SBU and a square linker. It is the most common topology, when possible, as the Zr_6 cluster is fully saturated with the maximum number of carboxylates it can accommodate. However, studies have shown that for this to be possible, the torsion angle between the carboxylates with the backbone (core) of the linker needs to be close to $0°$.[19] As the linkers used in this work have two sp^3 carbons, the pyrazole and phenyl rings are out of the plane formed by the carbon of the carboxylic groups. As the carboxylates are conjugated with the aromatic rings they are attached to, they are going to be out of that plane too, making the **ftw** topology very unlikely. This is evidenced by analysis of the MOF structures reported in this work; none of the structures have the carboxylates in plane with the core of the linker, and thus ruling out the **ftw** topology (Fig. S23, ESI†). The hypothetical structure for the ligands arranged in the **ftw** topology also shows significant strain based on observation of the framework structure. This strain may be partially offset by the fully saturated cluster, but this does not represent a likely framework product. If the linkers adopted a tetrahedral geometry, **ith** could also be possible. However, this topology is rare, as it is challenging to form a cuboctahedra SBU with a tetrahedral linker; the single example reported was obtained as a byproduct and could not be obtained phase pure.[60]

Since the **ftw** and **ith** topologies are unlikely products, we turned our attention to evaluating the topologies that can be formed with a tetratopic linker and the 8-connected (cubic) Zr-SBU. The combination of a tetratopic linker and a cubic SBU can lead to four different topologies: **csq**, **scu**, **sqc** and **flu**.

The energetics of the framework formation for all different linkers in the possible topologies suggest the **csq** topology is lowest in energy for L1 and TCPE and the **scu** topology for L2 (Table S2, ESI†). However, there does not appear to be a large difference in the relative energies for each of the topologies and this suggests all are likely for the three linkers. Notably we find the spread of energies becomes significantly lower in TCPE (~ 0.005 eV per atom) compared to L1 (~ 0.1 eV per atom) demonstrating that larger more flexible ligands can provide access to a greater range of topologies than smaller, more rigid, ligands.

As noted, all three linkers contain two sp^3 carbons, and they can adopt either a tetrahedral or square planar conformation. In the case where the linker adopts a tetrahedral conformation, only one topology is expected: **flu**. This is observed in UAM-11 due to the conformational flexibility of the central phenyl group, allowing L2 to adopt a "tetrahedral-like" conformation with a torsion angle of $60°$ between all four carboxylates forming a distorted **flu** topology. It is not clear why L2 prefers to adopt a tetrahedral conformation over a square planar conformation, but one hypothesis is that the small energy difference between the different HCCH dihedral angles observed in the study of the free ligand means that it does not favour any specific angle within the MOF that is formed. Consequently, we hypothesize that **flu** could be favoured because, out of the four topologies considered, **flu** is the only topology that does not form channels, and rather it forms a more rigid and stable structure with large pores accessible only through smaller pore apertures. While other topologies for L2 based MOFs might be accessible based on the simulation data, attempts to induce the formation these by altering the synthetic conditions were unsuccessful, resulting in the production of either amorphous powders or the same **flu** topology.

When the linker adopts a square/rectangular planar geometry, instead of a tetrahedral geometry, this can lead to the formation of three possible topologies: **csq**, **scu**, and **sqc**, as documented in literature.[8] Normally, the **csq** topology is more commonly observed compared to **scu** and **sqc**. Surprisingly, none of the MOFs formed in our study had the **csq** topology despite this being predicted to be energetically possible (further discussion below); however, our simulation approach did not consider the possibility of coordinating molecules that may act to bridge proximal Zr nodes which is observed in the **scu** topology, particularly for L1 (Fig. S7, ESI†).

Ligand L1 is observed to form UAM-10, where the framework adopts an **scu** topology, while TCPE provides MOFs UAM-1000 and UAM-1002, which adopt **sqc** and **scu** topologies, respectively. Analysis of structures shows that the adoption of an *anti*-conformation and thereby a more rectangular linker results in an **scu** topology, whereas a *syn* conformation (and more square linker) leads to the **sqc** topology. This small difference in linker conformation looks to be important, as the **scu** topology normally forms with rectangular ligands while for the **sqc** topology appears to prefer a more square arrangement, albeit the latter is based on only two reported examples. Comparing UAM-1000 and UAM-1002 shows that the orientation of the
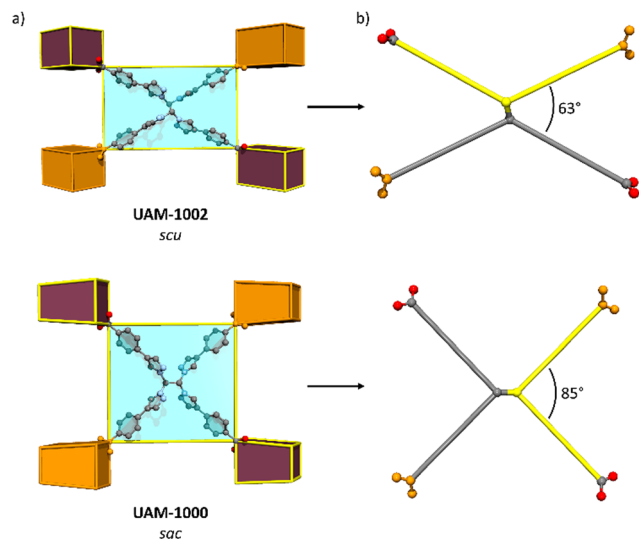
Fig. 4 (a) Representations of the **scu** (top) and **sqc** (bottom) MOF topologies showing the linker orientation and disposition that allows it to be connected to four cubic clusters that are in the same orientation. (b) Schematic representation of the linkers highlighting in the same colour the two arms that are attached to the same carbon of the central ethylene group.

metal clusters and the carboxylates of the ligand are the same in both UAM-1002 and UAM-1000 with the only difference being that in UAM-1000 the ligand has squarer dimensions and in UAM-1002 more rectangular (Fig. 4). Simulations of hypothetical frameworks based on different ligand conformations of L1 and TCPE support these observations (Table S3, ESI†).

Finally, as noted, we have observed that the **csq** topology (*e.g.*, NU-1000 type materials) cannot be obtained with any of the linkers studied. In general, the **csq** topology tends to be favoured more with square linkers, while **scu** topology is favoured with more rectangular linkers, which is consistent with our observations in UAM-10 and UAM-1002. We hypothesize that while the linkers L1 and TCPE can adopt a squarer arrangement (seen for the latter in UAM-1000) they may be too flexible to form a **csq** topology with such large pores, consistent with its absence in this work.

Post-synthetic metalation of the MOFs

To evaluate the ability of the bis-pyrazole units in UAM-10, UAM-11, UAM-1000, and UAM-1002 undergo PSMet, we examined reactions conducted with a relatively inert metal (minimal leaching) that could induce an easily detectable colour change in the crystals. $PdCl_2$ was chosen for this purpose. Metalation of UAM-1000 with $PdCl_2$ was recently investigated by us.[28] Partial metalation (*ca.* 50% PSMet) was achievable at the bis-pyrazole units due to the proximity of the adjacent bis-pyrazole unit, which hindered full metalation for steric reasons. The flexibility of the linker TCPE also posed challenges for determining the structure by SCXRD, but this could be overcome by incorporating a secondary linker to create UAM-1001, where the material was effectively locked.

Considering that UAM-10 and UAM-11 have shorter ligands compared to UAM-1000, we anticipated that these compounds would be easier to metalate in a single crystal-to-single crystal manner and characterise the outcome by SCXRD. However, attempts to PSMet UAM-10 and UAM-11 with $PdCl_2$ was unsuccessful. SEM-EDX analysis revealed some Pd present (Table S4, ESI†); however, the metalation was inconsistent across the sample and between samples, and SCXRD analysis revealed the pyrazoles to still be in an *anti*-conformation. Given that UAM-10 and UAM-11 have linkers with the pyrazoles directly attached to carboxylate groups and exhibit an *anti*-conformation of the bis-pyrazole units in the as-synthesised form of the MOF, these results suggest there is a significant barrier to convert from *anti* to *syn* within the MOF. This is likely due to this *anti* to *syn* change requiring a significant geometric and structure metric change in the linker that cannot be tolerated by the MOF topology.

In contrast, heating crystals of UAM-1002 in an acetonitrile solution of $PdCl_2$ resulted in a colour change of the crystals to the typical orange colour of bis-pyrazole coordinated Pd(II) (Fig. S25, ESI†). SEM-EDX analysis confirmed the presence of Pd(II) in the MOF, with a Zr:Pd ratio of 3:2 for UAM-1002 (Table S4, ESI†), consistent with full metalation of the bis-pyrazole sites. This is a notable contrast to UAM-1000, which due to the short 5.3 Å separation between two the two bis-pyrazole groups, only allows 50% metalation with $PdCl_2$ under similar conditions. As UAM-1002 has shown significant structural flexibility (PXRD and gas adsorption data) we also expected the crystals to diffract poorly. To our surprise, the toluene-solvated crystals (formed by solvent exchange) diffracted very well and SCXRD analysis of a crystal of UAM-1002[PdCl_2] confirmed that the Pd(II) metal centre was bound to the bis-pyrazole units in a typical square planar geometry, with two chlorides completing the coordination sphere (Fig. 5). Interestingly, compared to as-synthesised UAM-1002, the Zr-clusters where now significantly closer in the *c*-axis and bridged by formate anions (Fig. 5(a)) transforming its structure from a dot-type to a rod-type of MOF (with a different topology to the parent structure).[4] We hypothesize that when chelating the Pd(II) centre, the pyrazoles switch from *anti* to *syn* (facilitated by the phenyl spacer in the ligand arms decoupling this motion from the carboxylates, compare with UAM-10 and UAM-11) and the overall ligand changes its donor disposition to a more anisotropic shape, which forces the Zr nodes closer. The proximity of the nodes allow the formate capping ligands to change from chelating the Zr-clusters to bridging them, in turn providing more rigidity to the structure and allowing a better quality diffraction.

Conclusions

In summary, we have reported a study into the formation of Zr-MOFs formed from flexible tetratopic pyrazole carboxylate linkers. Two new linkers have been reported (L1H_4 and L2H_4) and the formation of three new Zr-MOFs (UAM-10, UAM-11 and
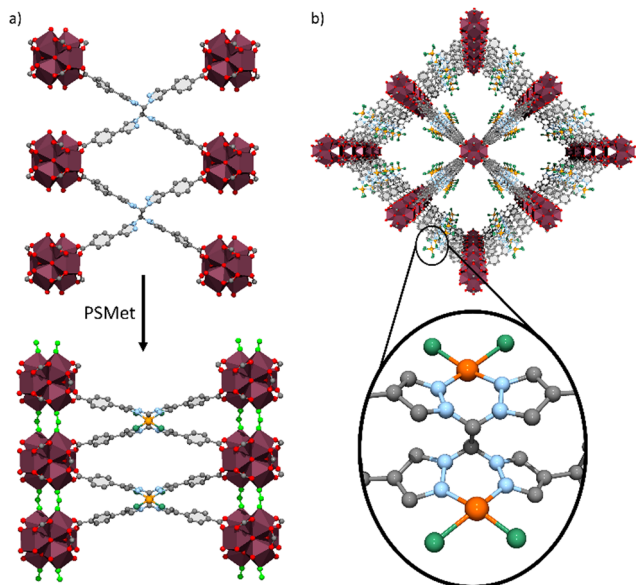
2366 | *J. Mater. Chem. C*, 2024, **12**, 2359–2369

This journal is © The Royal Society of Chemistry 2024

Fig. 5 (a) Representations of ligands bound to the Zr clusters in UAM-1002 (top) and UAM-1002[PdCl$_2$] (bottom). The transition from *anti*-(top) to *syn*-conformation (bottom) brings the Zr-clusters close enough that they end up being bridged by formate anions (represented in light green). (b) Representation of the structure of UAM-1002[PdCl$_2$] along the *c* axis, with the enlargement showing the PdCl$_2$ complex bound to the bis-pyrazole groups with a square planar geometry.

UAM-1002) observed. The combination of our experimental observations and simulations reveals that when using flexible pyrazole carboxylate linkers in the synthesis of Zr-MOFs the overall linker length and width (phenyl spacers within the arms) affects the accessible conformations of the linker, thereby limiting or allowing the synthesis of particular MOF topologies. Narrower linkers like L1H$_4$ are more conformationally restricted, allowing access to a single topology while wider linkers like TCPE allow synthesis of different topologies by fine tuning of the synthetic conditions. For example, the reaction of TCPE and ZrCl$_4$ in DMF and TFA form an **sqc** topology while the reaction in DEF and formic acid forms the **scu** topology. Interestingly, when TCPE adopts a *syn*-conformation the **sqc** topology appears to be preferred and when it adopts an *anti*-conformation it forms the **scu** topology. Interestingly, this is the first time that the **sqc** topology was observed to be the dominant phase among 8,4 connected topologies, whereas typically the **csq** topology is encountered. L2H$_4$ is somewhat unique in that it has significant conformational freedom yet still forms only one MOF structure preferentially. We hypothesize the formation of the uncommon sqc topology, rather than the **scu** and **csq**, is favoured for flexible tetracarboxylate linkers that have a square arrangement of the donors. Alternative topologies, such as **csq**, may represent unstable frameworks considering the size of the channels in this topology.

The length and width of the linker not only affects the topologies that can be formed but also the ability of the bis-pyrazolyl groups to transition from an *anti*- to a *syn*-conformation. Shorter and rigid linkers disfavour the transition

preventing PSMet, as observed with UAM-10 and UAM-11. Wider linkers like TCPE allow easier transition from an *anti* to a *syn*-conformation as the carboxylate and pyrazole core of the ligand is decoupled, allowing PSMet. Consequently, UAM-1002 possesses the right flexibility to allow structural changes upon PSMet and the elucidation of the inserted organometallic complex. These properties, combined with large unidirectional channels make UAM-1002 a great platform that could be exploited as a crystalline sponge for the study of the chemistry that occurs at the anchored organometallic complexes.

Author contributions

The manuscript was written through contributions of all authors. All authors have given approval to the final version of the manuscript.

Conflicts of interest

There are no conflicts to declare.

Acknowledgements

Notes and references

1 P. M. Bhatt, V. Guillerm, S. J. Datta, A. Shkurenko and M. Eddaoudi, *Chem*, 2020, **6**, 1613–1633.

2 P. Deria, D. A. Gómez-Gualdrón, I. Hod, R. Q. Snurr, J. T. Hupp and O. K. Farha, *J. Am. Chem. Soc.*, 2016, **138**, 14449–14457.

3 Z.-J. Li, Y. Ju, X.-L. Wu, X. Li, J. Qiu, Y. Li, Z.-H. Zhang, M.-Y. He, L. Zhang, J.-Q. Wang and J. Lin, *Inorg. Chem. Front.*, 2023, **10**, 1721–1730.

4 F. M. Amombo Noa, M. Abrahamsson, E. Ahlberg, O. Cheung, C. R. Göb, C. J. McKenzie and L. Öhrström, *Chem*, 2021, 7, 2491–2512.

5 I. Kurzydym and I. Czekaj, *Tech. Trans.*, 2020, **117**, 1–24.

6 M. C. Wasson, C. T. Buru, Z. J. Chen, T. Islamoglu and O. K. Farha, *Appl. Catal., A*, 2019, **586**, 117214.

7 Z. Chen, K. O. Kirlikovali, P. Li and O. K. Farha, *Acc. Chem. Res.*, 2022, **55**, 579–591.

8 H. Jiang, D. Alezi and M. Eddaoudi, *Nat. Rev. Mater.*, 2021, **6**, 466–487.

9 O. M. Yaghi, M. O'Keeffe, N. W. Ockwig, H. K. Chae, M. Eddaoudi and J. Kim, *Nature*, 2003, **423**, 705–714.

10 Z. Chen, J. Weseliński, K. Adil, Y. Belmabkhout, A. Shkurenko, H. Jiang, P. M. Bhatt, V. Guillerm, E. Dauzon, D.-X. Xue, M. O'Keeffe and M. Eddaoudi, *J. Am. Chem. Soc.*, 2017, **139**, 3265–3274.

11 Z. Chen, S. L. Hanna, L. R. Redfern, D. Alezi, T. Islamoglu and O. K. Farha, *Coord. Chem. Rev.*, 2019, **386**, 32–49.

12 M. J. Kalmutzki, N. Hanikel and O. M. Yaghi, *Sci. Adv.*, 2018, **4**, eaat9180.

13 D. Sun, S. Ma, J. M. Simmons, J.-R. Li, D. Yuan and H.-C. Zhou, *Chem. Commun.*, 2010, **46**, 1329–1331.

14 E. Biemmi, S. Christian, N. Stock and T. Bein, *Microporous Mesoporous Mater.*, 2009, **117**, 111–117.

15 G.-Y. Qiao, S. Yuan, J. Pang, H. Rao, C. T. Lollar, D. Dang, J.-S. Qin, H.-C. Zhou and J. Yu, *Angew. Chem., Int. Ed.*, 2020, **59**, 18224–18228.

16 D. Feng, Z. Y. Gu, J. R. Li, H. L. Jiang, Z. Wei and H. C. Zhou, *Angew. Chem., Int. Ed.*, 2012, **51**, 10307–10310.

17 J. H. Cavka, S. Jakobsen, U. Olsbye, N. Guillou, C. Lamberti, S. Bordiga and K. P. Lillerud, *J. Am. Chem. Soc.*, 2008, **130**, 13850–13851.

18 C. Koschnick, M. W. Terban, R. Frison, M. Etter, F. A. Böhm, D. M. Proserpio, S. Krause, R. E. Dinnebier, S. Canossa and B. V. Lotsch, *J. Am. Chem. Soc.*, 2023, **145**, 10051–10060.

19 R. Luebke, Y. Belmabkhout, Ł. J. Weseliński, A. J. Cairns, M. Alkordi, G. Norton, Ł. Wojtas, K. Adil and M. Eddaoudi, *Chem. Sci.*, 2015, **6**, 4095–4102.

20 J. Ma, L. D. Tran and A. J. Matzger, *Cryst. Growth Des.*, 2016, **16**, 4148–4153.

21 J. Pang, S. Yuan, J. Qin, C. Liu, C. Lollar, M. Wu, D. Yuan, H.-C. Zhou and M. Hong, *J. Am. Chem. Soc.*, 2017, **139**, 16939–16945.

22 J. Lyu, X. Zhang, K.-I. Otake, X. Wang, P. Li, Z. Li, Z. Chen, Y. Zhang, M. C. Wasson, Y. Yang, P. Bai, X. Guo, T. Islamoglu and O. K. Farha, *Chem. Sci.*, 2019, **10**, 1186–1192.

23 Y. Chen, X. Zhang, M. R. Mian, F. A. Son, K. Zhang, R. Cao, Z. Chen, S.-J. Lee, K. B. Idrees, T. A. Goetjen, J. Lyu, P. Li, Q. Xia, Z. Li, J. T. Hupp, T. Islamoglu, A. Napolitano, G. W. Peterson and O. K. Farha, *J. Am. Chem. Soc.*, 2020, **142**, 21428–21438.

24 H.-L. Xia, K. Zhou, L. Yu, H. Wang, X.-Y. Liu, D. M. Proserpio and J. Li, *Inorg. Chem.*, 2022, **61**, 7980–7988.

25 T. Islamoglu, K.-I. Otake, P. Li, C. T. Buru, A. W. Peters, I. Akpinar, S. J. Garibay and O. K. Farha, *CrystEngComm*, 2018, **20**, 5913–5918.

26 H.-Q. Xu, K. Wang, M. Ding, D. Feng, H.-L. Jiang and H.-C. Zhou, *J. Am. Chem. Soc.*, 2016, **138**, 5316–5320.

27 H.-L. Jiang, D. Feng, K. Wang, Z.-Y. Gu, Z. Wei, Y.-P. Chen and H.-C. Zhou, *J. Am. Chem. Soc.*, 2013, **135**, 13934–13938.

28 P. Gimeno-Fonquernie, J. Albalad, J. D. Evans, J. R. Price, C. J. Doonan and C. J. Sumby, Submitted 2023.

29 C. J. Coghlan, C. J. Sumby and C. J. Doonan, *CrystEngComm*, 2014, **16**, 6364–6371.

30 E. A. Nudnova, A. S. Potapov, A. I. Khlebnikov and V. D. Ogorodnikov, *Russ. J. Org. Chem.*, 2007, **43**, 1698–1702.

31 H. Cao, Z. Liu and Q. Wang, *Polym. Chem.*, 2017, **8**, 3810–3814.

32 P. Pracht, F. Bohle and S. Grimme, *Phys. Chem. Chem. Phys.*, 2020, **22**, 7169–7192.

33 C. Bannwarth, S. Ehlert and S. Grimme, *J. Chem. Theory Comput.*, 2019, **15**, 1652–1671.

34 S. Ehlert, M. Stahn, S. Spicher and S. Grimme, *J. Chem. Theory Comput.*, 2021, **17**, 4250–4261.

35 J. Keupp and R. Schmid, *Faraday Discuss.*, 2018, **211**, 79–101.

36 A. K. Rappe, C. J. Casewit, K. S. Colwell, W. A. Goddard and W. M. Skiff, *J. Am. Chem. Soc.*, 1992, **114**, 10024–10035.

37 P. G. Boyd, S. M. Moosavi, M. Witman and B. Smit, *J. Phys. Chem. Lett.*, 2017, **8**, 357–363.

38 A. P. Thompson, H. M. Aktulga, R. Berger, D. S. Bolintineanu, W. M. Brown, P. S. Crozier, P. J. in 't Veld, A. Kohlmeyer, S. G. Moore, T. D. Nguyen, R. Shan, M. J. Stevens, J. Tranchida, C. Trott and S. J. Plimpton, *Comput. Phys. Commun.*, 2022, **271**, 108171.

39 J. P. Perdew, K. Burke and M. Ernzerhof, *Phys. Rev. Lett.*, 1996, **77**, 3865–3868.

40 S. Goedecker, M. Teter and J. Hutter, *Phys. Rev. B: Condens. Matter Mater. Phys.*, 1996, **54**, 1703–1710.

41 S. Grimme, J. Antony, S. Ehrlich and H. Krieg, *Chem. Phys.*, 2010, **132**, 154104.

42 J. Vandevondele, M. Krack, F. Mohamed, M. Parrinello, T. Chassaing and J. Hutter, *Comput. Phys. Commun.*, 2005, **167**, 103–128.

43 T. D. Kühne, M. Iannuzzi, M. Del Ben, V. V. Rybkin, P. Seewald, F. Stein, T. Laino, R. Z. Khaliullin, O. Schütt, F. Schiffmann, D. Golze, J. Wilhelm, S. Chulkov, M. H. Bani-Hashemian, V. Weber, U. Borštnik, M. Taillefumier, A. S. Jakobovits, A. Lazzaro, H. Pabst, T. Müller, R. Schade, M. Guidon, S. Andermatt, N. Holmberg, G. K. Schenter, A. Hehn, A. Bussy, F. Belleflamme, G. Tabacchi, A. Glöß, M. Lass, I. Bethune, C. J. Mundy, C. Plessl, M. Watkins, J. Vandevondele, M. Krack and J. Hutter, *Chem. Phys.*, 2020, **152**, 194103.

44 T. F. Willems, C. Rycroft, M. Kazi, J. C. Meza and M. Haranczyk, *Microporous Mesoporous Mater.*, 2012, **149**, 134–141.

45 T. M. McPhillips, S. E. McPhillips, H. J. Chiu, A. E. Cohen, A. M. Deacon, P. J. Ellis, E. Garman, A. Gonzalez, N. K. Sauter, R. P. Phizackerley, S. M. Soltis and P. Kuhn, *J. Synchrotron Radiat.*, 2002, **9**, 401–406.

46 N. P. Cowieson, D. Aragao, M. Clift, D. J. Ericsson, C. Gee, S. J. Harrop, N. Mudie, S. Panjikar, J. R. Price, A. Riboldi-Tunnicliffe, R. Williamson and T. Caradoc-Davies, *J. Synchrotron Radiat.*, 2015, **22**, 187–190.

47 D. Aragao, J. Aishima, H. Cherukuvada, R. Clarken, M. Clift, N. P. Cowieson, D. J. Ericsson, C. L. Gee, S. Macedo, N. Mudie, S. Panjikar, J. R. Price, A. Riboldi-Tunnicliffe,

2368 | *J. Mater. Chem. C*, 2024, **12**, 2359–2369

This journal is © The Royal Society of Chemistry 2024

R. Rostan, R. Williamson and T. T. Caradoc-Davies, *J. Synchrotron Radiat.*, 2018, **25**, 885–891.

48 G. M. Sheldrick, *Acta Crystallogr. Sect., A: Found. Crystallogr.*, 2015, **71**, 3–8.

49 G. M. Sheldrick, *Acta Crystallogr. Sect., A: Found. Crystallogr.*, 2008, **64**, 112–122.

50 G. M. Sheldrick, *Acta Crystallogr. Sect., C: Cryst. Struct. Commun.*, 2015, **71**, 3–8.

51 L. J. Barbour, *Supramol. Chem.*, 2001, **1**, 189–191.

52 O. V. Dolomanov, L. J. Bourhis, R. J. Gildea, J. A. K. Howard and H. Puschmann, *J. Appl. Crystallogr.*, 2009, **42**, 339–341.

53 A. L. Spek, *Acta Crystallogr., Sect. C: Cryst. Struct. Commun.*, 2015, **71**, 9–18.

54 K. Dr. H. Putz, Dr. K. Brandenburg GbR, Diamond – Crystal and Molecular Structure Visualization – Crystal Impact, 53227, Bonn, Germany, 1999, 102.

55 R. A. Peralta, M. T. Huxley, R. J. Young, O. M. Linder-Patton, J. D. Evans, C. J. Doonan and C. J. Sumby, *Faraday Discuss.*, 2021, **225**, 84–99.

56 Y. Liu, J. H. Her, A. Dailly, A. J. Ramirez-Cuesta, D. A. Neumann and C. M. Brown, *J. Am. Chem. Soc.*, 2008, **130**, 11813–11818.

57 W. M. Bloch, C. J. Doonan and C. J. Sumby, *CrystEngComm*, 2013, **15**, 9663.

58 L. Chen, J. P. S. Mowat, D. Fairen-Jimenez, C. A. Morrison, S. P. Thompson, P. A. Wright and T. Düren, *J. Am. Chem. Soc.*, 2013, **135**, 15763–15773.

59 S. Amirjalayer and R. Schmid, *J. Phys. Chem. C*, 2008, **112**, 14980–14987.

60 H. Furukawa, F. Gándara, Y.-B. Zhang, J. Jiang, W. L. Queen, M. R. Hudson and O. M. Yaghi, *J. Am. Chem. Soc.*, 2014, **136**, 4369–4381.

This journal is © The Royal Society of Chemistry 2024

J. Mater. Chem. C, 2024, **12**, 2359–2369 | **2369**